An Intermediate-Age α-Rich Galactic Population Beyond the Solar Neighborhood

A Senior Honors Thesis

Presented in Partial Fulfillment of the Requirements for Graduation *with Honors Research Distinction* in Astronomy in the Undergraduate Colleges of The Ohio State University

By

Jack T. Warfield

The Ohio State University

April 2020

Project Advisors: Professors Marc H. Pinsonneault & Jennifer A. Johnson, Department of Astronomy

Abstract

Understanding the chemical history of the Galaxy is essential for developing theories and models for our Galaxy's formation history. I expanded on the results of previous work studying the relationship between chemical composition and age in the Kepler field using a new sample of red giant stars that were observed during NASA's K2 mission. This sample of stars that I used is distributed along 3 different lines of sight and reaches much further into the Galaxy than the Kepler field does. Therefore, analysis of these K2 fields allows us to see whether the composition and age trends that are observed in the solar neighborhood are also true everywhere else. Current theory suggests that the trends in the Kepler field should be true at large, as the composition of the interstellar medium at a given point in the Galaxy's history should primarily be dependent on when Type Ia and core-collapse supernova begin to go off. I selected the targets used in this analysis based on the availability of APOGEE DR16 spectra and of masses derived from the asteroseismic parameters in the K2 Galactic Archaeology Project Data Release 2. To do this analysis, I wrote a program that finds ages for individual stars by interpolating within a grid created from a set of stellar evolutionary tracks that were generated based on theoretical stellar models. This program returns the main sequence lifetime of a star provided its mass and chemical composition. I have been able to recover the age trends that were found for stars in the Kepler field while also showing that, by considering a star's alpha enhancement, this method for finding ages is an improvement over methods used in previous literature as it corrects underestimates of the ages of low-mass stars. When applied to the stars in the K2 fields, I have not recovered this trend, and instead have identified a population of stars rich in alpha elements with intermediate ages (6-9 billion years). The existence of this population is very hard to explain with our current models of Galaxy formation.

Contents

Chapter 1: The Bi-Modal Alpha Sequence 3

Chapter 2: Finding Stellar Ages 7

2.1 General Principles 7

2.2 Catalogs and Selecting a Sample 8

2.3 Sample Age Determination 11

Chapter 3: Results and Discussion 17

Chapter 1: The Bi-Modal Alpha Sequence

The bi-modal α sequence of stars in the Galaxy is still a puzzle. This sequence was noted by e.g. Bensby et al. (2003) who showed that there are distinct trends in [α/Fe] vs. [Fe/H] space for the geometrically defined thin and thick discs (Gilmore & Reid 1983). Hayden et al. (2015) investigated how these trends behave as a function of Galactic radius (R) and height above the Galactic plane (Z) using 69,919 red giants from APOGEE DR12. These authors found the high-α part of this sequence to only be strongly present at $|Z| > 0.5$ kpc and $R < 11$ kpc.

Bensby et al. (2003) attributed this bi-modality to be a product of the historic supernova rates. Type Ia supernovae (SNe Ia) come from exploding white dwarfs and contribute a significant percentage of iron to the interstellar medium (ISM). Type II supernovae (SNe II), also known as core-collapse supernovae, occur at the end of the lives of massive stars and are the primary source of α elements (oxygen, magnesium, silicon, sulfer, calcium, and titanium) in the Galaxy. Since massive stars would have been formed at the beginning of star formation in the Galaxy and these stars have relatively short lifetimes, SNe II would have therefore been contributing to the ISM almost immediately, resulting in a population of stars from the first few billion years of star formation with a very high proportion of α elements to iron. SNe Ia, on the other hand are linked to the timescale to form the first white dwarfs and therefore would not contribute to the ISM until relatively recently in the Galaxy's history. Once these began to heavily contribute, however, the ISM would have been quickly enriched with iron, leading to the second population of younger stars with high [Fe/H] and lower (near solar) [α/Fe].

Accurate ages for stars in these two chemical populations observed by NASA's Kepler satellite were calculated by Silva Aguirre et al. (2018). Partially motivated by finding chemical signatures that can be used as tracers of the thin and thick discs, these authors used a combination of photometric, spectroscopic, and asteroseismic parameters to estimate the ages of 1590 red giants and red clump stars located within the Kepler field. They found that the population of giants with low [α/Fe] are described by a kernal density function that peaks at $\sim$2 Gyr and slopes gradually down to older ages, where the population with high [α/Fe] peaks strongly at $\sim$11 Gyr. The ages of these populations were found to have limited overlap, with a transition at $\sim$8 Gyr. Overall, these results agree very well with what might be expected if only considering the contribution of historic SNe rates to the ISM. However, the application of these results to these chemical populations in general rather than just the solar circle is still relatively uncertain, as giants in the Kepler field were only targeted for asteroseismology out to distances of about 2 kpc.

Because of the origins of these elements, it is true that these populations must be somehow tied to the history of SNe II and Ia. However, there are likely other mechanisms also at play contributing to the formation of this chemical and age pattern. One of these possible mechanisms is the radial migration of stars mixing together populations of different chemical origins. In this scenario, the range of metallicities that is observed for the low-α locus is not interpreted to be showing the evolution of a single population but rather is formed from the superposition of the endpoints from the different mixed populations. Stars born in different pockets of gas throughout the Galaxy are born at different parts in these tracks over the Galaxy's history. When mixed together, they form the sequence that we are familiar with. Therefore, the primary explanation for the lack of an age-metallicity relation is mostly attributed to stars' neighbors not having necessarily been birthed out of the same gas as stars have moved radially inwards adn outwards in their orbits (see e.g. Schönrich & Binney 2009; Weinberg et al. 2017; Nidever et al. 2014).

Another possible explanation is that these two loci are the products of two gas infall episodes that both spurred two independent periods of stellar formation. In this scenario, the high-α sequence was formed during a rapid infall episode that happened about 10 billion years ago. This would be followed by a drought of star formation that would itself be followed by a gradual infall episode spurring star formation from about 8 Gyr ago to present (Chiappini et al. 1997). Each of these star formation episodes would drive historic rates of SNe II, but have lesser effects on changing the rate of SNe Ia. Spitoni et al. (2019), simulating this "two-infall" scenario, were able to successfully replicate the bi-modal α sequence as well as the age trends found in Silva Aguirre et al. (2018) for the high- and low-α sequences.

A third mechanism that could be responsible for this sequence is if η(t)—the ratio of the rate of the outflow of metal-rich gas from the Galaxy to the rate at which metal-rich gas is incorporated into stars—increased in value at some point in the Galaxy's history. In this scenario, the low-α sequence would form first followed by the high-α sequence after a transition to a higher value of η. Weinberg et al. (2017) shows that the bi-modal sequence can be recreated in a model where η increases from about 1.5 to 8 with a transition time at 4 Gyr. Though capable of recreating the bi-modal αsequence, this mechanism seems unlikely to be at least the dominant contributor knowing the results from Silva Aguirre et al. (2018) and the links between these chemical populations and the thin and thick disks.

A fourth mechanism is that the bi-modal sequence is the product of star formation happening in clumpy bursts throughout the Galaxy. In this scenario, there is a background of star formation within the low-α sequence and the rest of the star formation takes place in gas-rich clumps that naturally arose in the disc. When star formation is spurred in these clumps, these populations of stars are initially enriched with α elements via the SNe mechanisms described above. Therefore, in this scenario, the high-α sequence is formed from a superposition of these clumpy star formation

episodes (see e.g. Clarke et al. 2019). Assuming that the populations are not mixed together (perhaps via radial migration), this allows nearly identical chemical populations observed in different regions of the Galaxy to have diverging ages.

Chapter 2: Finding Stellar Ages

2.1 General Principles

Essentially no matter what technique is being used, finding ages for red giants starts with having some sort of mass or mass analog. The time that a star spends burning hydrogen on the main sequence is tied to the amount of fuel—and therefore mass—that it has to burn. Therefore, detailed stellar evolution models, given a star's mass and composition, are able to self-consistently estimate what the main-sequence lifetime of a star must be. After leaving the main sequence, stars that do not have cores hot enough to immediately begin burning helium will move onto the red giant branch. The time that a star spends on the red giant branch is only on the order of a hundred million years. Since the main source of error in our estimates will be on the mass from the random and systematic errors in $\nu_{\rm max}$ and $\Delta\nu$, and these errors propagate to being around 30% in age, finding the main-sequence lifetimes of these red giant stars is an accurate age probe at their total ages for this population analysis. Therefore, obtaining accurate, self-consistent ages for red giant stars is primarily dependent on having accurate estimates for stellar mass and secondarily on harmoniously-calibrated values for chemical compositions.

A set of stellar evolutionary tracks can be expressed as a grid that returns what the present main-sequence age of a star must be based on "observed" parameters such as mass and composition. Because these tracks form a discrete grid, numerical techniques must be applied to use it to find general results. If a grid is finely-sampled enough, it may be appropriate to simply select the closest point in the grid to the

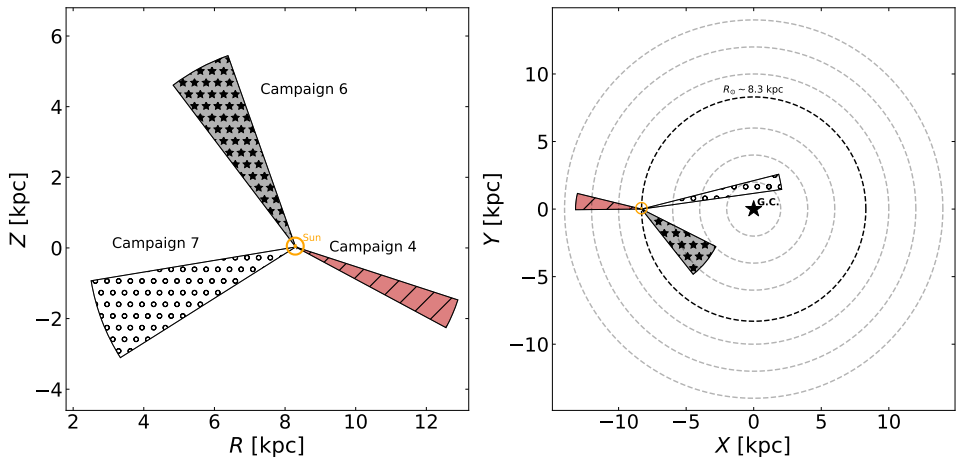

Figure 2.1: Schematics showing the approximate lines of sight for K2 campaigns 4, 6, and 7. The plot on the right shows the fields in the Galactocentric coordinates Z (height above or below the Galactic plane) and R (radial distance from the Galactic center). The plot on the right shows these fields in the Galactocentric X and Y coordinates. The sun is approximated to be at $R = 8.3$ kpc, $Z = 0.027$ kpc, $X = 8.3$ kpc, and $Y = 0$ kpc.

values for a given star. Otherwise, it is necessary to employ some sort of interpolation technique in order to estimate lookup-values in the grid.

2.2 Catalogs and Selecting a Sample

My catalog of stars was created through the combination of the K2 Galactic Archaeology Project Data Release 2 (K2GAP DR2; Zinn et al., in preparation) and the 16th Data Release of the Sloan Digital Sky Survey's Apache Point Obsevatory Galactic Evolution Experiment (APOGEE DR16; Ahumada et al. 2019). K2GAP DR2 contains values for the asteroseismic parameters of $\nu_{\rm max}$ (the oscillation frequency of maximum power) and $\Delta\nu$ (the mean large frequency separation) for giant stars observed during K2 campaigns 4, 6, and 7, as well as radii derived from Gaia DR2 photometry (Gaia Collaboration et al. 2016, 2018; Zinn et al. 2019). These three campaigns were chosen as they probe three lines of sight that are both distinct from each

other and from the Kepler field (figure 2.1). Additionally, campaigns after campaign 3 benefit from an improvement in the K2 photometry. These asteroseismic parameters are the products of six independent pipelines that analyze time-series power spectra of the K2 light curves for signatures of oscillations. We only consider giants in this catalog for which at least two of these pipelines returned values for both $\nu_{\rm max}$ and $\Delta\nu$ and use the mean of these values.

The spectroscopic data in APOGEE DR16 were collected with the 2.5-meter Sloan Foundation Telescope at the Apache Point Observatory in New Mexico and the 2.5-meter du Pont Telescope at Las Campanas Observatory in Chile as a part of SDSS-IV (Blanton et al. 2017). APOGEE DR16 contains values for stellar and chemical composition, such as [Fe/H] and [α/M][1], along with values for stellar parameters such as effective temperature ($T_{\rm eff}$) and surface gravity (g). These values are obtained by processing the spectra through the APOGEE Stellar Parameters and Chemical Abundances Pipeline (ASPCAP) which infers these values by fitting the spectra to a grid of synthetic spectra (for a description of the pipeline, see García Pérez et al. 2016).

I reduced the subset of stars with both K2GAP and APOGEE DR16 data to stars that were determined to most likely be red giant stars based on an asteroseismically-calibrated spectroscopic classification. I used stars in the APOKASC-2 catalogue (Pinsonneault et al. 2018) that are classified as red giants in Elsworth et al. (2019) to fit for the parameters α, β, and γ that help define a "reference" temperature given by

$$T_{\rm ref} = \alpha + \beta\,[{\rm Fe/H}]_{\rm RAW} + \gamma\,(\log{(g)}_{\rm SPEC} - 2.5), \tag{2.1}$$

where $[{\rm Fe/H}]_{\rm RAW}$ and $\log{(g)}_{\rm SPEC}$ are the uncorrected values given for metallicity and surface gravity, respectively, in the APOGEE DR16 catalogue. These were found to

[1] [α/Fe] and [α/M] are conceptually equivalent, with the [α/M] parameter used by APOGEE measuring the ratio of α elements to the overall metallicity rather than just to iron.

Table 2.1: Grid for if a star is classified as a red giant for different ranges of $\log(g)_{\rm SPEC}$ and [C/N]. [C/N] and [Fe/H] refer to the uncalibrated values for the carbon to nitrogen ratio and metallicty. Stars are classified as red giants if the statement for the given range of conditions is true for that star. $\Delta T = T_{\rm eff}^{\rm SPEC} - T_{\rm ref}$.

	$3.5 > \log(g)_{\rm SPEC} > 2.38$	$\log(g)_{\rm SPEC} < 2.38$
[C/N] > -0.30	[C/N] $< 0.02 - 0.54$[Fe/H] $- 0.003\Delta T$	True
[C/N] < -0.30	$150 > 182.66$[Fe/H] $+ \Delta T$	True

have approximate values of $\alpha = 4383.148$ K, $\beta = -235.136$ K/dex, and $\gamma = 532.659$ K. A line was then fit through the approximate ridgeline in $[{\rm C/N}]_{\rm RAW}$ vs. $T_{\rm eff}^{\rm SPEC} - T_{\rm ref}$ space for which 98% of stars to the right of the line were classified as red giants. The finalized classification criteria are listed in table 2.1.

From the parameters provided by K2GAP and APOGEE, I was able to calculate values for asteroseismic surface gravity ($\log(g)_{\rm seis}$), for mass, and for radius. $\log(g)_{\rm seis}$ was calculated using $\nu_{\rm max}$ and $T_{\rm eff}$ in the scaling relation (Brown et al. 1991):

$$\nu_{\rm max} \propto g\, T_{\rm eff}^{-1/2}, \tag{2.2}$$

with solar reference values of $\nu_{\rm max,\odot} = 3076$ μHz, $T_{\rm eff,\odot} = 5772$ K, and $g_\odot = 27400$ cm/s^2 (cite?). Values for mass and radius can be found by combining equation 2.2 with the scaling relation for $\Delta\nu$ (Ulrich 1986),

$$\Delta\nu \propto M^{1/2} R^{-3/2}. \tag{2.3}$$

Doing this gives that

$$M \propto \nu_{\rm max}^3 T_{\rm eff}^{3/2} \Delta\nu^{-4} \tag{2.4}$$

and

$$R \propto \nu_{\rm max} T_{\rm eff}^{1/2} \Delta\nu^{-2}. \tag{2.5}$$

The sample was then further limited to stars with [α/M] values between 0.0 and 0.4 dex and [Fe/H] values between -2.0 and 0.6 dex. In addition, I included distances that were found using Gaia parallaxes with the method of Bailer-Jones (2015). Each star's height above the Galactic plane (Z) and radial distance from the center of the Galaxy (R) was computed from these distances and the each stars' right ascension and declination using the `galpy`[2] package (Bovy 2015).

My sample is divided into the two groups of luminous and low-luminosity giants based on a cut in surface gravity. Because luminous giants have shorter oscillation frequencies, there is a significant amount of error in the astroseismic measurements for these stars due to the relatively short dwell times of the K2 campaigns. Stars with $\log(g)_{\rm seis} < 2.5$ are classified as luminous giants and stars with $\log(g)_{\rm seis} > 2.5$ are classified as low-luminosity giants.

Lastly, the sample was divided into the categories of α-rich and α-poor by approximately drawing a line through the ridge-line between the two populations, as seen in figure 2.3.

2.3 Sample Age Determination

To find age estimates for my sample I used stellar evolutionary tracks from Tayar et al. (2017) that were generated with the Yale Rotating Evolution Code (Pinsonneault et al. 1989; van Saders & Pinsonneault 2012). From these tracks I created three sets of grids at the $\log(g)$'s of 3.30, 2.50, and 1.74, with columns for $\log$(Mass), [Fe/H], [α/Fe], and $\log$(age). These values for $\log(g)$ were chosen as what approximately bracket the low-luminosity giants (3.30 and 2.50) and the upper giant branch (2.50 and 1.74). We made these grids regular along the $\log$(Mass), [Fe/H], and [α/Fe] axes by linearly interpolating to ages at locations where there were gaps in the tracks.

[2]http://www.galpy.org/

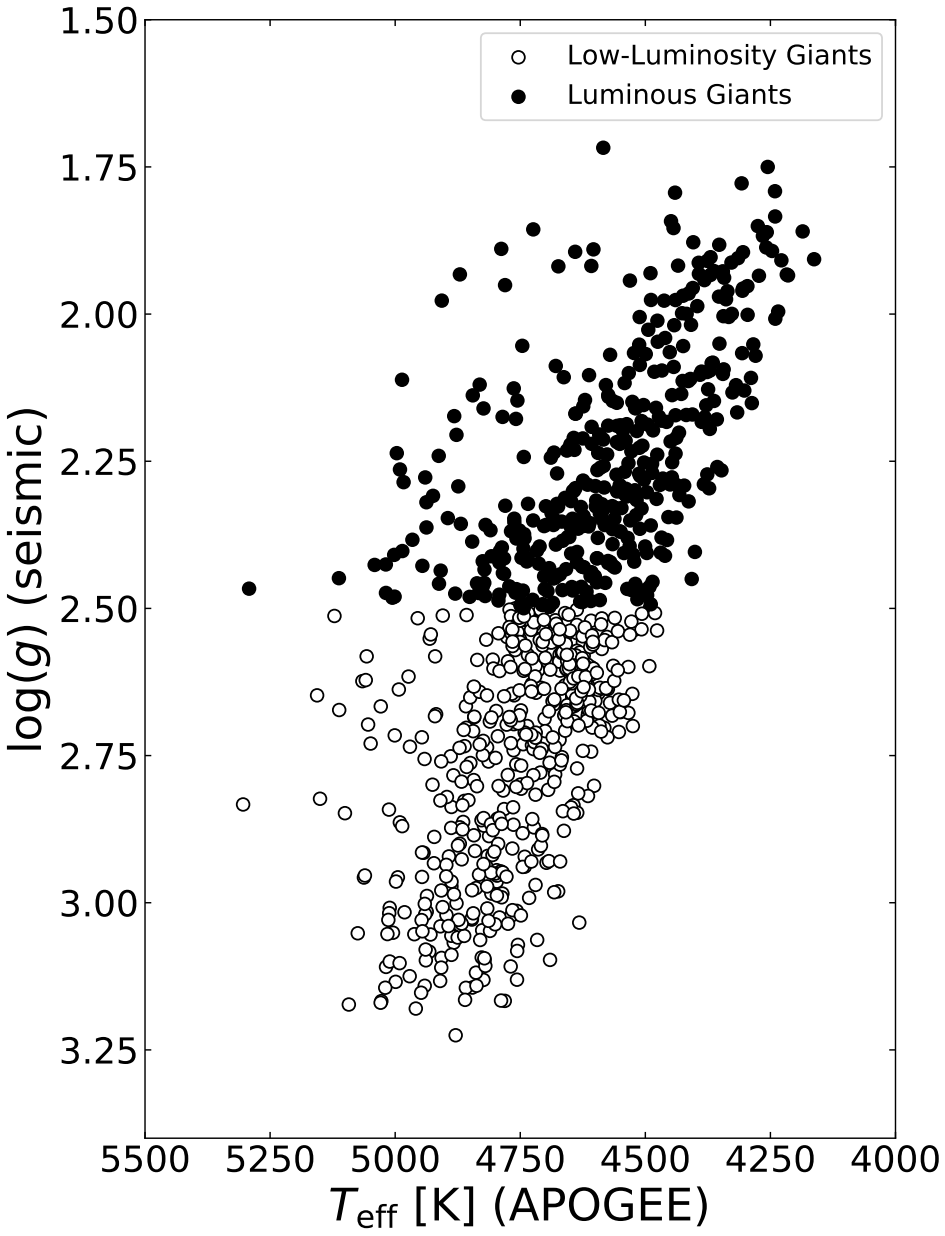

Figure 2.2: Kiel diagram for our sample of stars using effective temperatures from APOGEE and surface gravities calculated from the K2GAP DR2 astereoseismic parameters and APOGEE effective temperatures. Low-luminosity giants are defined here as giants with $\log(g) > 2.5$.

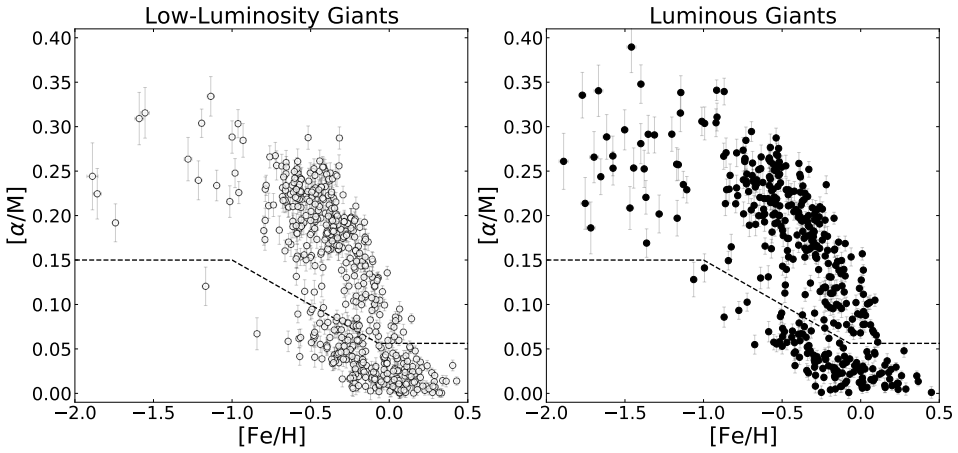

Figure 2.3: [α/M] vs. [Fe/H] for the low-luminosity and luminous giants in our sample. Our sample is further split into the categories of α-rich and α-poor, which is defined by the dashed line in the plots. This division was defined by-eye based on the ridge-line between the groups of points in the data. This cut is similar to that made by e.g. Silva Aguirre et al. (2018) and Weinberg et al. (2019). This line is defined as $y = 0.15$ for $x < -1.0$, $y = 0.056$ for $x > -0.07$, and $y = -0.1x + 0.049$ for $-1.0 < x < -0.07$.

The interpolation method that I used to estimate an age given the parameters for a star was four-dimensional four-point Lagrange interpolation. In two dimensions, four-point Lagrange interpolation works by fitting the interpolation Lagrange polynomial given by the equation

$$L(x) = \sum_{j=0}^{3} y_j \ell_j(x), \tag{2.6}$$

where

$$\ell_j(x) = \prod_{\substack{0 \leqslant m \leqslant 3 \\ m \neq j}} \frac{x - x_m}{x_j - x_m} \tag{2.7}$$

are the Lagrange basis polynomials. This is calculated for a set of four ordered pairs $(x_0, y_o), \ldots, (x_3, y_3)$. This equation gives an estimate for values of $y = L(x)$ for any given x between x_0 and x_3 while keeping that $L(x_j) = y_j$.

This can be expanded to more dimensions. For this work, I am considering the four-tuples $(x, y, z, w) = (\log M, [\text{Fe/H}], [\alpha/\text{Fe}], \log \tau)$. I can fit a set of four four-tuples that surround our star's values for x, y, and z with the interpolation polynomial

$$L(x, y, z) = \sum_{j=0}^{3} \sum_{k=0}^{3} \sum_{m=0}^{2} w_{j,k,m} \ell_j(y) \ell_k(z) \ell_m(w). \tag{2.8}$$

The one exception is y. Since the tracks from Tayar et al. (2017) only samples three values for $[\alpha/\text{Fe}]$, $(y_0, y_1, y_2) = (0.0, 0.2, 0.4)$ always.

Given a star's values and associated errors for each of these parameters, a Monte Carlo method was used to calculate 300 age estimates for each star with equation 2.8. The reported results for a given star is the median of these values and the standard deviation calculated from the median absolute deviation[3].

As a test of my method, figure 2.4 shows a comparison between the ages calculated for 2641 red giants in the Kepler field using this method and the ages reported

[3] $\sigma \approx 1.4826 \times \text{MEDIAN}(|\tilde{x} - x|)$

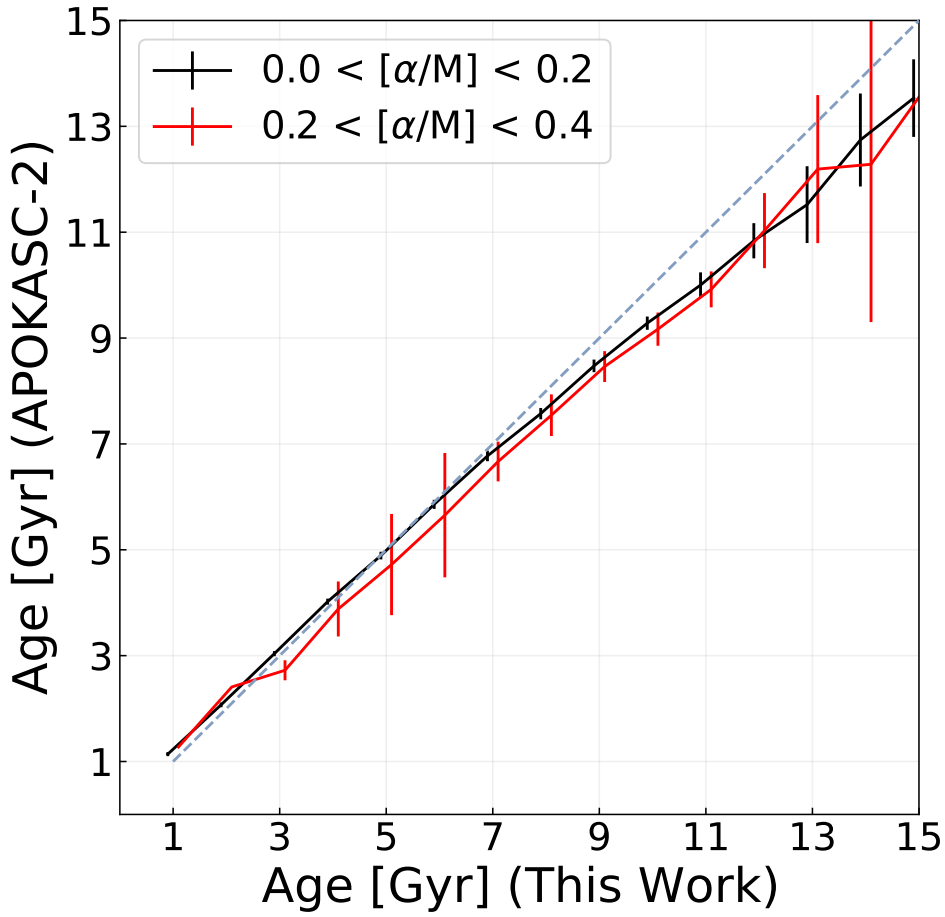

Figure 2.4: A comparison of the ages reported in the APOKASC-2 catalog vs. the ages calculated using our method for 928 low-α and 400 high-α giants randomly drawn from the APOKASC-2 catalog. The number of stars randomly drawn from each category is proportional to the total number of stars in each category.

for the same giants in the APOKASC-2 catalog. From this figure it is apparent that the ages we found trend slightly older. This is due to the fact that, though Pinsonneault et al. used a similar "grid-based" method to estimate the ages of these stars, the stellar tracks and isochrones used did not take a star's [α/Fe] into account, meaning that these are the ages that these stars would have if they were at solar α-enhancements. This has an effect of underestimating the ages of low-mass stars with [α/Fe] > 0.

Chapter 3: Results and Discussion

The panels in figure 3.1 show the age results from both the Kepler and K2 fields. Results are shown for both the full samples and for the low-luminosity giants in each field. Figure 3.2 shows these same results for each K2 campaign individually. Gaussian kernal density functions were drawn over each distribution using the `kdeplot` function from the `seaborn`[1] Python package. We can see that, though the inclusion of the luminous giants does not have a significant impact on the locations of the peaks for the underlying kernel density estimates they do add a noticeable degree of scatter to the results. Table 3.1 summarizes these results for the α-rich giants in each field.

Comparing our results for these K2 fields with the results from the Kepler field brings to light two interesting differences. First, though the median age of the α-rich population is strongly peaked at a single age in both of these samples, the populations in the K2 fields are found to be at an age about 2 Gyr younger than what was found in the Kepler field. Secondly, there seems to be much less of a divergence between the ages of the α-rich and α-poor populations in the K2 field. Lian et al. (2020) discuss a population of young, α-rich stars in the outer disk, suggesting that there should have also been mechanisms in place to make this intermediate age population. It is also interesting to note that the ages of these two populations seem to converge as a function of height above the Galactic plane, a trend that is shown in figure 3.3. Hayden et al. (2017) notes a similar convergence in their sample, where coeval populations of α-rich and α-poor stars are found to have the same vertical scale heights.

[1] https://seaborn.pydata.org/

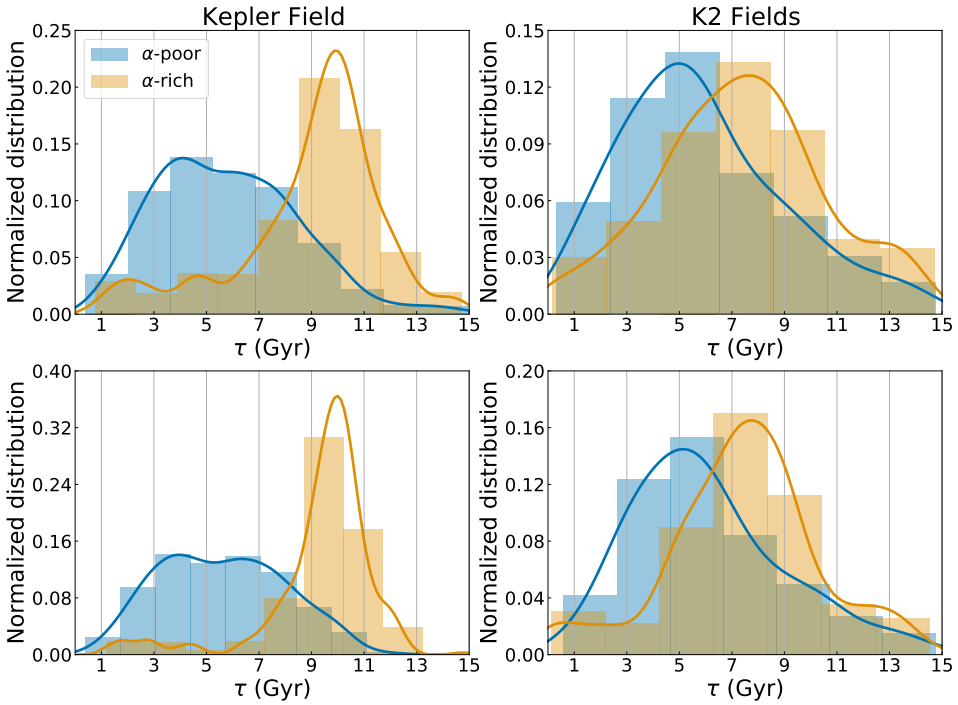

Figure 3.1: Distributions of the age estimates for the Kepler field (left) and K2 fields (right) for both the α-poor and α-rich populations. The top row of figures show the distributions for the full sample for the respective fields and the bottom row shows the distributions for the low-luminosity sample ($\log(g)_{\rm seis} > 2.5$).

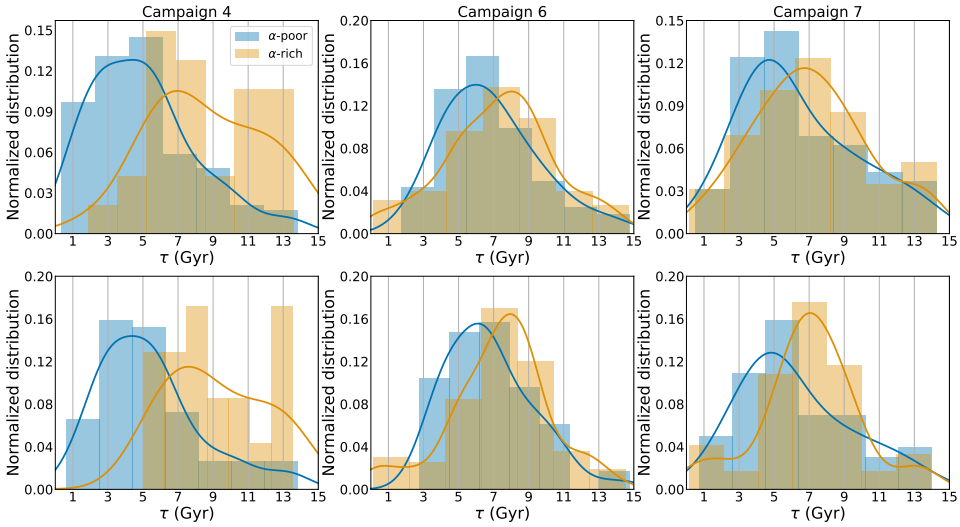

Figure 3.2: Distributions of the age estimates for both the α-poor and α-rich populations for each K2 field individually. The top row of figures show the distributions for the full sample for the respective fields and the bottom row shows the distributions for the low-luminosity sample ($\log(g)_{\rm seis} > 2.5$).

Table 3.1: This table gives information for the kernal density estimation (kde) and underlying data for the age-distributions of the α-rich populations in each field. The value for σ is calculated as $\sigma = \mathrm{FWHM}/2.355$, where FWHM is the full width at half maximum around the peak in the kde. The mean error is the average error in the age estimate for only the α-rich stars in the indicated field.

Field	α-rich peak age (Gyr)	α-rich σ (Gyr)	α-rich mean error (Gyr)
Kepler	9.86	1.22	1.82
K2 C4	6.93	4.16	2.81
K2 C6	7.99	2.59	2.57
K2 C7	6.80	3.19	2.59
all K2	7.67	2.76	2.59

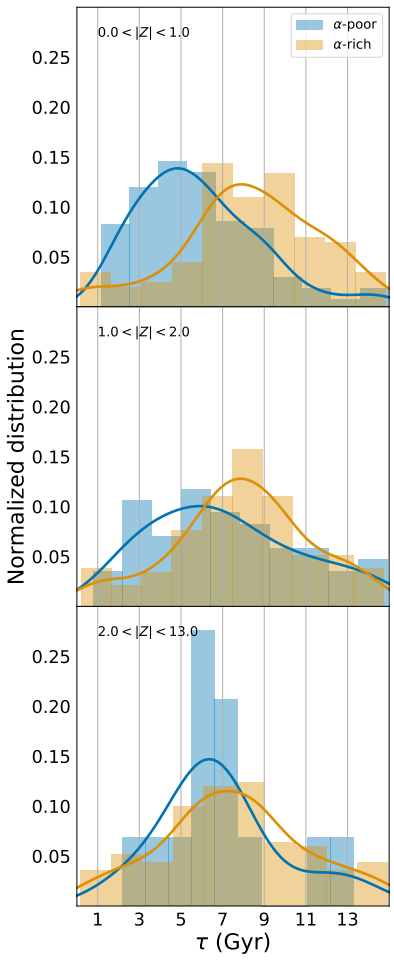

Figure 3.3: Distributions of the age estimates for both the α-poor and α-rich of the K2 fields for 1 kpc bins in Z. Where the median age of the α-rich population is about constant as a function of vertical height, the α-poor population seems to increase in age as $|Z|$ increases, with the populations converging on an age of about 7-8 Gyr.

However, with these results in hand, we can begin to look back at our methods for generating the bi-modal αsequence to see how these results fit with the various hypotheses. Because of the strong peaks in the ages of these populations in the K2 fields versus the Kepler field, there seems to be a lack of the mixing of populations that you would expect from radial migration. Additionally, as they were presented here, these results—along with the previous results in the Kepler field—seem to contradict the scenario of an evolving $\eta(t)$. The ages of the α-rich populations in K2 as compared to this population in Kepler suggests that the two-infall scenario would have to be slightly more complex if star formation happened at different times in different places in the Galaxy. Perhaps the most likely explanation that was presented is the model of clumpy star formation. However, in this scenario, it is still curious why only the very local Galaxy is unique in its star formation history in comparison to anywhere else that we look.

Looking forward, the third data release of the K2 Galactic Archaeology Program will provide us with asteroseismic data for giants along sixteen more lines of sight in the Galaxy. Additionally, a similar analysis is possible with data from NASA's ongoing Transiting Exoplanet Survey Satellite (TESS) mission. This data, along with the spectroscopy from the final APOGEE data releases and from other large-scale surveys, can be utilized to fill in a more complete picture of the age gradients for stellar populations throughout the Milky Way.

References

Ahumada, R., Allende Prieto, C., Almeida, A., et al. 2019, arXiv e-prints

Bailer-Jones, C. A. L. 2015, PASP, 127, 994

Bensby, T., Feltzing, S., & Lundström, I. 2003, A&A, 410, 527

Blanton, M. R., Bershady, M. A., Abolfathi, B., et al. 2017, AJ, 154, 28

Bovy, J. 2015, ApJS, 216, 29

Brown, T. M., Gilliland, R. L., Noyes, R. W., & Ramsey, L. W. 1991, ApJ, 368, 599

Chiappini, C., Matteucci, F., & Gratton, R. 1997, ApJ, 477, 765

Clarke, A. J., Debattista, V. P., Nidever, D. L., et al. 2019, MNRAS, 484, 3476

Elsworth, Y., Hekker, S., Johnson, J. A., et al. 2019, MNRAS, 489, 4641

Gaia Collaboration, Prusti, T., de Bruijne, J. H. J., et al. 2016, A&A, 595, A1

Gaia Collaboration, Brown, A. G. A., Vallenari, A., et al. 2018, A&A, 616, A1

García Pérez, A. E., Allende Prieto, C., Holtzman, J. A., et al. 2016, AJ, 151, 144

Gilmore, G., & Reid, N. 1983, MNRAS, 202, 1025

Hayden, M. R., Recio-Blanco, A., de Laverny, P., Mikolaitis, S., & Worley, C. C. 2017, A&A, 608, L1

Hayden, M. R., Bovy, J., Holtzman, J. A., et al. 2015, ApJ, 808, 132

Lian, J., Thomas, D., Maraston, C., et al. 2020, arXiv e-prints

Nidever, D. L., Bovy, J., Bird, J. C., et al. 2014, ApJ, 796, 38

Pinsonneault, M. H., Kawaler, S. D., Sofia, S., & Demarque, P. 1989, ApJ, 338, 424

Pinsonneault, M. H., Elsworth, Y. P., Tayar, J., et al. 2018, ApJS, 239, 32

Schönrich, R., & Binney, J. 2009, MNRAS, 396, 203

Silva Aguirre, V., Bojsen-Hansen, M., Slumstrup, D., et al. 2018, MNRAS, 475, 5487

Spitoni, E., Silva Aguirre, V., Matteucci, F., Calura, F., & Grisoni, V. 2019, A&A, 623, A60

Tayar, J., Somers, G., Pinsonneault, M. H., et al. 2017, ApJ, 840, 17

Ulrich, R. K. 1986, ApJ, 306, L37

van Saders, J. L., & Pinsonneault, M. H. 2012, ApJ, 746, 16

Weinberg, D. H., Andrews, B. H., & Freudenburg, J. 2017, ApJ, 837, 183

Weinberg, D. H., Holtzman, J. A., Hasselquist, S., et al. 2019, ApJ, 874, 102

Zinn, J. C., Pinsonneault, M. H., Huber, D., et al. 2019, ApJ, 885, 166